UNIVERSIDAD DISTRITAL
FRANCISCO JOSÉ DE CALDAS

Ingeniería

https://revistas.udistrital.edu.co/index.php/reving/issue/view/1350

DOI: https://doi.org/10.14483/23448393.24404

Research

Unified Model for Inverter-Based Microgrids: A Methodology

Modelo unificado para microrredes basadas en inversores: una metodología

Alonso Chica-Leal [1]*, César L. Trujillo [1], and Francisco Santamaría [1]

[1]Universidad Distrital Francisco José de Caldas, Bogotá, Colombia

Abstract

Context: The behavior of inverter-based microgrids during transitions between grid-connected and islanded modes is critical to stability and power quality. Most small-signal models treat each regime separately or rely on heuristic switching logic, which complicates the consistent analysis of mode transitions. This work introduces a unified hybrid dynamic model that captures both operating modes and the synchronization constraints imposed at the point of common coupling.
Method: A step-by-step methodology is proposed in which a reduced dynamic-phasor representation of the grid and loads, small-signal models of droop-controlled inverters, and linearized power relations around operating points are combined. These components are assembled into a single state-space model valid in both grid-connected and islanded operation and embedded into a hybrid system with hysteresis and minimum dwell time for the static transfer switch (STS). Under a time-scale separation assumption, mode-by-mode linearizations are evaluated using eigenvalue-based metrics and a common quadratic Lyapunov-function test. The closed-loop PCC impedance is computed to characterize whether the controlled converters exhibit predominantly resistive or inductive behavior.
Results: A laboratory-scale microgrid with two three-phase inverters and a resistive–inductive load is considered. Planned islanding and reconnection events are simulated in Matlab/HyEQ Toolbox. Well-damped power transients are obtained, with PCC frequency deviations below 0,07 Hz and PCC voltage deviations below 0,5 Vrms. STS closing actions occur with phase mismatch below 1◦ and without power overshoot.
Conclusions: The unified hybrid model provides a single framework for analyzing both operating regimes and their transitions. It enables systematic tuning of droop and synchronization parameters and provides a practical basis for future extensions to weaker grids, nonlinear loads, and hardware-in-the-loop validation.
Keywords: Droop control, dynamic phasors, hybrid dynamical systems, microgrid, parallel inverters

Article history

Received:
Nov 18th, 2025

Modified:
Dec 10th, 2025

Accepted:
Feb 4th, 2026

Ing, vol. 31, no. 2, 2026. e24404

©The authors; reproduction right holder Universidad Distrital Francisco José de Caldas.

CC BY NC SA

*Correspondence: ajchical@udistrital.edu.co

Resumen

Contexto: El comportamiento de las microrredes basadas en inversores durante las transiciones entre los modos de operación conectada a la red e isla es crítico para la estabilidad y la calidad de la potencia. La mayoría de los modelos de pequeña señal tratan cada régimen por separado o recurren a lógicas de conmutación heurística, lo que dificulta un análisis consistente de las transiciones. En este trabajo se presenta un modelo dinámico híbrido unificado que representa ambos modos de operación e incorpora las restricciones de sincronización impuestas en el punto de acoplamiento común (PCC).
Metodología: Se propone una metodología paso a paso que combina una representación fasorial dinámica reducida de la red y las cargas, modelos de pequeña señal de inversores con control por caída (*droop control*), y relaciones de potencia linealizadas alrededor de puntos de operación. Estos componentes se integran en un único modelo de espacio de estados válido para los modos de conexión a la red e isla, que posteriormente se incorpora a un sistema dinámico híbrido con histéresis y un tiempo mínimo de permanencia en el interruptor estático de transferencia. Bajo el supuesto de separación de escalas de tiempo, las linealizaciones por modo se evalúan mediante métricas de autovalores y una prueba de una función de Lyapunov cuadrática común. Asimismo, se calcula la impedancia cerrada en el PCC para caracterizar el comportamiento de los convertidores controlados como fuentes predominantemente resistivas o inductivas.
Resultados: Se considera una microrred a escala de laboratorio compuesta por dos inversores trifásicos y una carga resistivo–inductiva. Se simulan eventos planificados de formación de isla y reconexión en Matlab con la herramienta HyEQ. Se obtienen transitorios bien amortiguados, con desviaciones de frecuencia en el PCC menores a $0{,}07$ Hz, desviaciones de tensión menores a $0{,}5$ $\mathrm{V_{rms}}$ y cierres del interruptor estático con desajuste de fase inferior a $1°$, sin sobreimpulsos de potencia.
Conclusiones: El modelo híbrido unificado proporciona un marco común para analizar ambos regímenes y sus respectivas transiciones. Además, permite realizar una sintonización sistemática de los parámetros de caída y sincronización, y constituye una base práctica para futuras extensiones hacia redes débiles, cargas no lineales y validación experimental de hardware en el lazo.

Palabras clave: Control por caída, fasores dinámicos, sistemas dinámicos híbridos, microrred, inversores en paralelo

1. Introduction

The deployment of electronic converters has increased significantly in recent years, driven largely by the growing integration of distributed energy resources (DERs) and energy storage systems. By locating DERs closer to the point of demand, the need for extensive electric transmission infrastructure can be reduced. An islanded or grid-connected system within a defined area that integrates and coordinates DERs is referred to as a microgrid (MG) [1, 2]. DERs typically interfaced with the MG through power electronic converters, particularly voltage-sourced inverters (VSIs) [3, 4].

Extensive research has been conducted on the modeling and control of parallel inverter-based microgrids capable of operating in both grid-connected and islanded modes. Each operating mode exhibits distinct dynamic characteristics and imposes different control requirements and technical regulations necessary for the loads, or to maintain a load balance between generation and load. Effective

management of these systems is therefore essential for maintaining stability, efficiency, and reliability as MGs become increasingly important in modern power systems.

Various modeling methods are employed for both small-signal [4–7] and large-signal [2] operation of microgrids in grid-connected and islanded modes. Methods used to obtain the small-signal voltage and frequency dynamics of the inverters include classical phasor models [6], dynamic phasor models [5], and synchronous-reference-frame models based on Clarke and Park transformations [4]. These approaches differ in how they represent the system components and the MG-to-grid interconnection; the appropriate choice depends on the objectives of the study. For large-signal analysis, Kirchhoff's laws and appropriate coordinate transformations can be applied without linearization, resulting in a nonlinear model with fewer fitting errors. For small signals, an averaged model is linearized around an operating point, and it is therefore valid only locally.

The literature reveals a lack of unified models capable of capturing both grid-connected and islanded operation modes within a single framework. To address this gap, this work proposes a unified model for MGs based on hybrid dynamical systems (HDS) theory.

HDS modeling approach has been extensively applied across various domains, including robotics, manufacturing, biological systems, healthcare, renewable energy integration, power electronics, cyber-physical systems, aerospace, and automotive industries. However, comprehensive HDS models specifically developed for microgrids remain relatively scarce. Recent studies have focused on analyzing trajectory sensitivity and switching events in power-electronic microgrids using experimental and modeling methodologies [6, 8]. Other studies have examined stochastic components and operational uncertainties during islanding and reconnection [7, 9]. For instance, in [10], an AC microgrid is modeled as an HDS, and a hybrid controller operating across three distinct time scales is designed together with a large-signal stability analysis. Despite these advancements, a gap remains in the development of a unified model that seamlessly integrates islanded and grid-connected modes, including the transitional and pre-synchronization phases between them.

Microgrids can be controlled to pursue active- and reactive-power goals using linear and nonlinear mathematical models of physical components, including inverters, DERs, batteries, loads, and the electrical grid. Several control techniques have been proposed, including droop control, proportional-integral-derivative (PID) control, model predictive control (MPC), sliding-mode control, LQ-Servo control, or machine-learning–based control [1, 2, 4, 11, 12].

Microgrid control can be achieved with or without communication links. However, the inclusion of communication systems tends to increase costs and introduces additional dependence on communication reliability. Alternatively, communication-less primary control relies on local measurements at each inverter; droop control is a representative example [2, 4, 12].

The small-signal stability of inverter-based microgrids has been extensively analyzed using linearized models, eigenvalue plots, and frequency-domain tools specifically designed for droop-controlled systems [5, 7, 10]. Most of these studies concentrate on a single operating mode, either grid-connected or islanded, and examine aspects such as damping margins, critical poles, and the effects of control parameters on local stability [13]. Other research has employed dynamic-phasor or impedance-based representations to capture grid interactions and load dynamics more accurately, although these studies generally remain limited to a single-mode analysis.

Seamless transitions between grid-connected and islanded operation have been investigated

from several perspectives, including PLL-based synchronization, soft transfer-switch strategies, and protection-oriented opening and reclosing logic at the point of common coupling (PCC) [8, 9]. Many of these contributions establish specific voltage, phase, and frequency thresholds for disconnection and reconnection and validate the proposed thresholds through time-domain simulations. Some approaches also incorporate small-signal analysis or Lyapunov-based methods to strengthen their findings.

In contrast, this work emphasizes a *unified* hybrid model that combines: (i) a common small-signal state space for both operating modes, (ii) explicit PCC switching logic with hysteresis and minimum dwell time, and (iii) an affine jump map that preserves incremental coordinates at STS commutations. This structure allows planned islanding and reconnection to be interpreted as trajectories of a single well-posed hybrid system $\mathcal{H} = (C, f, D, g)$, enabling the direct application of switched-system tools, such as Lie-algebraic and common quadratic Lyapunov function (CQLF) test, to the pair $\{A_{\text{sis}}^{\text{grid}}, A_{\text{sis}}^{\text{isl}}\}$ while keeping the seamless-transition constraints at the PCC explicit.

Scope. Throughout this paper, small-signal linearizations around mode-wise specific operating points are used. The inner current/voltage loops and PWM action are incorporated into the closed-loop matrices of each mode through a time-scale separation assumption; consequently, the hybrid supervisory logic and grid/droop couplings act on an *effective* linear plant for each mode. Large-signal, PWM-resolved validations are left for future work and do not affect the hybrid structure (C, f, D, g) presented here.

Section II presents the proposed methodology. Section III introduces the stability analysis of the unified hybrid model. Section IV describes the case study. Section V reports the simulation results. Section VI discusses the findings, and Section VII presents the conclusions.

The contributions of this work are threefold. First, a unified hybrid model is formulated to represent both islanded and grid-connected operation within a single state-space framework, explicitly incorporating the supervisory logic and synchronization constraints. Second, a methodology for controller assessment and stability certification is developed based on common quadratic Lyapunov arguments and quantitative indicators extracted from simulation trajectories. Third, a case study is conducted in which planned islanding and reconnection events are simulated, demonstrating bounded frequency, voltage, and phase deviations and confirming that smooth transitions without power overshoot can be achieved. These contributions distinguish the proposed approach from existing studies, in which operating modes are typically analyzed separately or the supervisory logic is not embedded within the dynamical model.

2. Proposed methodology

The microgrid (MG) is modeled as a hybrid system $\mathcal{H} = (C, f, D, g)$ following the framework proposed by Goebel, Sanfelice, and Teel [14]. The hybrid dynamics are given in Eq. (2.1):

$$\mathcal{H}: \qquad \begin{cases} \dot{z} = f(z), & z \in C, \\ z^{+} = g(z), & z \in D, \end{cases} \tag{2.1}$$

where the hybrid state is defined as

$$z := (x, m, \tau) \in \mathbb{R}^{n_x} \times \{0, 1\} \times \mathbb{R}_{\geq 0}.$$

x collects the continuous small-signal states (grid and inverters), $m \in \{0, 1\}$ is the state of the static transfer switch (STS) at the point of common coupling (PCC), with ($m = 0$: STS corresponding to the closed grid-connected mode and $m = 1$: STS to the open islanded mode, and τ is a dwell-time timer. The single-valued flow map is defined in Eq. (2.2).

$$f(z) = \begin{bmatrix} A_m\, x + B_m\, u_m \\ 0 \\ 1 \end{bmatrix}, \qquad z := (x, m, \tau), \tag{2.2}$$

where $A_m \in \mathbb{R}^{n_x \times n_x}$ and $B_m \in \mathbb{R}^{n_x \times n_u}$ are the mode-dependent state and input matrices assembled in Steps D–F. The state ordering and dimensions are fixed throughout the formulation: the first two states correspond to the grid-current components, followed by five states for each of the N inverters. Thus, $n_x = 2 + 5N$ (see Sec. H). The exogenous input u_m in Eq. (2.3) depends on the STS position:

$$u_m = \begin{cases} \mathbf{w}_{ur}, & m = 0 \text{ (STS closed, grid-connected)}, \\ \mathbf{0}, & m = 1 \text{ (STS open, islanded)}. \end{cases} \tag{2.3}$$

Here, $\mathbf{w}_{ur} = [\Delta e_{dg}\ \Delta e_{qg}]^\top$ denotes the small-signal PCC grid-voltage vector defined after the SLD in Fig. 1.

Incremental coordinates and affine jump map. Let $x^\star_m$ denote the operating point (OP) associated with mode $m \in \{0, 1\}$ (computed in Subsection G). During continuous flows, the *mode-wise incremental state* is defined by Eq. (2.4):

$$\tilde{x} \;:=\; x - x^\star_m, \tag{2.4}$$

This representation is used throughout the hybrid model. When a mode transition occurs, $m^+ = 1 - m$, the state is affinely realigned according to Eq. (2.5):

$$x^+ \;=\; x \;+\; \big(x^\star_{m^+} - x^\star_m\big), \qquad m^+ = 1 - m, \qquad \tau^+ = 0, \tag{2.5}$$

Consequently, the incremental state remains continuous across the switching event, as shown in Eq. (2.6):

$$\tilde{x}^+ \;=\; x^+ - x^\star_{m^+} \;=\; x - x^\star_m \;=\; \tilde{x}. \tag{2.6}$$

Thus, although the jump map is *affine in the absolute state* x, it does not induce electrical discontinuities. Instead, it changes the coordinate origin. The single-valued jump map can therefore be expressed compactly as in Eq. (2.7):

$$g(z) = \begin{bmatrix} x + (x^\star_{m^+} - x^\star_m) \\ m^+ \\ 0 \end{bmatrix}, \tag{2.7}$$

where $z := (x, m, \tau)$ denotes the hybrid state.

STS-based switching logic at the PCC. $\omega_{\text{rel}}, \theta_{\text{rel}}, E_{\text{rel}}$ denote the frequency, phase-angle, and voltage-magnitude mismatches between the utility grid and the PCC, respectively. These quantities are obtained from the voltage and current measurements available at the PCC through PT/CT

instrumentation. The STS is commanded to *open*, thereby transitioning to islanded operation ($m^+ = 1$), when the synchronization error exceeds an "open" threshold. Conversely, reconnection to the utility grid ($m^+ = 0$) is permitted when the synchronization error enters a more restrictive or tighter "close" window; in both cases a dwell time $\tau_{\min} > 0$ prevents chatter. Using the hysteretic functions defined in Eqs. (2.12a)–(2.12b), the flow/jump sets in Eqs. (2.13a)–(2.13b) implement this STS logic. At each jump, the map g toggles the STS mode according to $m^+ = 1 - m$, resets the timer to $\tau^+ = 0$, and preserves continuity of the electrical state through the x continuous.

Consistency with the SLD. In Fig. **1**, $m = 0$ (STS closed) activates the grid branch (R_{Lg}, L_g) and the exogenous input $\mathbf{w}_{ur}$; $m = 1$ (STS open) disconnects the branch and sets $\mathbf{w}_{ur} \equiv 0$ in the small-signal model.

PCC synchronization variables and thresholds (definitions). At the point of common coupling (PCC), let $\theta_{\mathrm{PCC}}(t)$ and $\omega_{\mathrm{PCC}}(t) = \dot{\theta}_{\mathrm{PCC}}(t)$ denote the local phase and frequency estimates, respectively. These quantities may be obtained from PT/CT measurements phase-locked loop (PLL), virtual PLL, or equivalent synchronization algorithm. Let $\theta_g(t),\ \omega_g(t)$ be the upstream grid references. The relative mismatches are defined in Eqs. (2.8)–(2.10):

$$\omega_{\mathrm{rel}} := \omega_{\mathrm{PCC}} - \omega_g, \tag{2.8}$$

$$\theta_{\mathrm{rel}} := \mathrm{wrap}_{[-\pi,\pi)}(\theta_{\mathrm{PCC}} - \theta_g)\,, \tag{2.9}$$

$$E_{\mathrm{rel}} := |V_{\mathrm{PCC}}| - |V_g|. \tag{2.10}$$

The hysteretic synchronization thresholds introduced in Eq. (2.11) satisfy

$$\omega_{\mathrm{close}} > 0,\ \ \omega_{\mathrm{open}} > \omega_{\mathrm{close}}, \qquad E_{\mathrm{close}} > 0,\ \ E_{\mathrm{open}} > E_{\mathrm{close}}, \qquad \theta_{\mathrm{close}} > 0, \tag{2.11}$$

together with the minimum dwell-time constraint $\tau_{\min} > 0$. Reconnection is permitted only within the tighter window $(\omega_{\mathrm{close}}, E_{\mathrm{close}}, \theta_{\mathrm{close}})$, whereas opening (islanding) uses the wider limits $(\omega_{\mathrm{open}}, E_{\mathrm{open}})$ as will be used in Eq. (2.12a). The threshold values are treated as design parameters and may be selected according to the applicable interconnection and protection requirements, thereby keeping the proposed formulation independent of a specific standard. The corresponding synchronization/error functions are defined as

$$\phi_{\mathrm{open}}(x) := \max\{\ |\omega_{\mathrm{rel}}| - \omega_{\mathrm{open}},\ \ |E_{\mathrm{rel}}| - E_{\mathrm{open}}\ \}, \tag{2.12a}$$

$$\phi_{\mathrm{close}}(x) := \min\{\ \omega_{\mathrm{close}} - |\omega_{\mathrm{rel}}|,\ \ E_{\mathrm{close}} - |E_{\mathrm{rel}}|,\ \ \theta_{\mathrm{close}} - |\theta_{\mathrm{rel}}|\ \}. \tag{2.12b}$$

Hence, an opening event is triggered when $\phi_{\mathrm{open}} \geq 0$, indicating that at least one opening criterion has been exceeded. Reconnection or a closing event is allowed when $\phi_{\mathrm{close}} \geq 0$, indicating that all metrics lie within the close window, provided that the dwell-time condition $\tau \geq \tau_{\min}$ is satisfied.

The flow and jump sets are therefore defined in Eqs. (2.13a)–(2.13b):

$$C = \{(x, 0, \tau) : \phi_{\mathrm{open}}(x) < 0\} \ \cup\ \{(x, 1, \tau) : \phi_{\mathrm{close}}(x) < 0\}, \tag{2.13a}$$

$$D = \{(x, 0, \tau) : \phi_{\mathrm{open}}(x) \geq 0,\ \tau \geq \tau_{\min}\} \ \cup\ \{(x, 1, \tau) : \phi_{\mathrm{close}}(x) \geq 0,\ \tau \geq \tau_{\min}\}. \tag{2.13b}$$

Since C and D are closed and the maps f and g are single-valued and locally Lipschitz on their respective domains, the hybrid basic conditions of [14] are satisfied. Hence, $\mathcal{H}$ in Eq. (2.1) is well posed and robust to small perturbations.

Observation (modeling coordinates). While Step D uses *dynamic phasors* to obtain the continuous map $x \mapsto A_m x + B_m u_m$ [5, 15], the framework is *coordinate–agnostic*: a conventional phasor model, a synchronous d–q (Clarke–Park) linearization [4], or even a large–signal nonlinear model [2] can be employed instead. The corresponding representation of line/filter parameters into A_m, B_m may change, but the hybrid structure (C, f, D, g) and the subsequent steps remain unchanged, provided that the reference directors and sign conventions are consistent.

Roadmap. Steps A–F build the common system and local models, whereas Steps G–I assemble the augmented state–space, compute operating points, and integrate the PCC logic into the hybrid model.

A. Technical characteristics and elements of the VSI-based MG

The nominal power, voltage, and frequency values; the number of inverters (N) participating in the MG; the relevant impedances; and the connection/disconnection mechanism used to change the operating mode are first specified.

B. Droop curve coefficients

The coefficients of the droop curves are calculated according to the inverter ratings and the voltage and frequency deviations permitted by the selected standard.

C. Prepare a single-line diagram (SLD)

The single-line diagram (SLD) adopted in this work is shown in Fig. **1**. The dashed vertical line marks the point of common coupling (PCC). A static transfer switch (STS), located at the PCC on the grid branch, enables the grid-connected operation; in islanded operation, the PCC is disconnected from the utility and supplies the local load. Each inverter $i = 1, \ldots, N$ is connected to the PCC through a feeder modeled by (R_{Li}, L_{Li}), with the reference current i_{Li} directed toward the PCC. The utility branch is modeled by (R_{Lg}, L_g) with i_{grid} defined into the PCC, whereas the islanded branch is modeled by $(R_{\text{Load}}, L_{\text{Load}})$ with i_{load} defined toward the load. Voltage and current measurement points (PT/CT) are placed at the PCC for droop and protection purposes.

Remark (alternative grid representations). The SLD is provided for illustrative purposes; any equivalent grid representation can be employed to construct the small-signal model in Step D. This includes options like a bus–branch formulation with a Y-bus matrix, an incidence representation, or explicit π/RL line models. The choice of representation determines how line or filter parameters are incorporated into $\mathbf{A}_{ur}, \mathbf{B}_{Uur}, \mathbf{B}_{Wur}$; the subscript "$ur$" indicates the coupling of inverter buses (u) and the remaining buses (r). The definitions of state and input, along with the subsequent steps, remain unchanged the same as long as the reference directions and sign conventions are consistently applied.

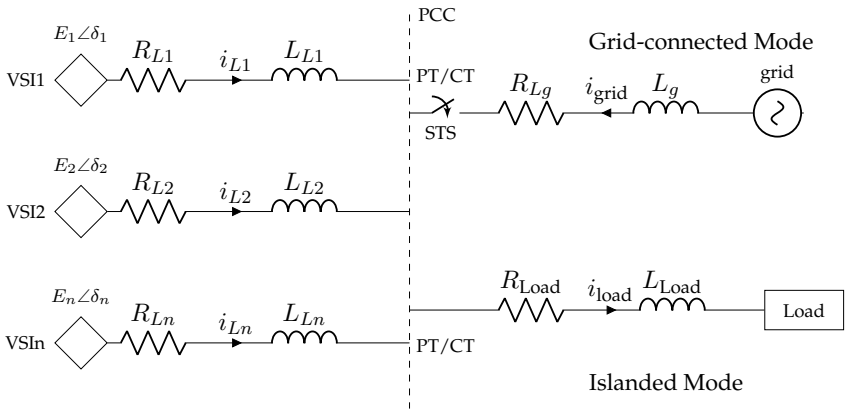

Figure **1**: **Step C** — Single-line diagram (SLD) highlighting the PCC and the static transfer switch (STS). Each inverter feeder includes (R_{Li}, L_{Li}). In grid-connected mode the STS ties the PCC to the utility branch (R_{Lg}, L_g) with i_{grid} defined into the PCC; in islanded mode the PCC feeds the local load $(R_{\text{Load}}, L_{\text{Load}})$ with i_{load} defined toward the load. PT/CT locations used by droop and protection are indicated.

PCC dq inputs (notation). In the synchronous d–q frame rotating at ω_0, let $e_{dg}(t), e_{qg}(t)$ denote the d/q components of the grid-side PCC voltage and let (E_{dg0}, E_{qg0}) denote their quiescent operating values. The small-signal deviations defined in Eqs. (2.14)–(2.15) are

$$\Delta e_{dg} := e_{dg} - E_{dg0}, \tag{2.14}$$

$$\Delta e_{qg} := e_{qg} - E_{qg0}. \tag{2.15}$$

The exogenous PCC input vector introduced in Eq. (2.16) is

$$\mathbf{w}_{ur} := \begin{bmatrix} \Delta e_{dg} \\ \Delta e_{qg} \end{bmatrix}, \tag{2.16}$$

which represents the grid-side voltage deviations entering the hybrid model. If the d-axis is aligned with the grid phasor at the operating point, then $E_{qg0} = 0$.

D. Grid-interconnection dynamics in grid-connected mode

The MG interconnection model in grid-connected operation is derived using dynamic phasors, following the formulation presented in [5]. Each inverter current is expressed in the synchronous d–q frame as $\Delta i_{d,n}$ and $\Delta i_{q,n}$, $n = 1, \ldots, N$, and the grid current as $\Delta i_{d,g}$ and $\Delta i_{q,g}$. Accordingly, the state vector is defined asEq. (2.17)

$$\mathbf{x}_{ur} = \left[\Delta i_{d,1}\ \Delta i_{q,1}\ \cdots\ \Delta i_{d,N}\ \Delta i_{q,N}\ \Delta i_{d,g}\ \Delta i_{q,g}\right]^\top \in \mathbb{R}^{2(N+1)}. \tag{2.17}$$

Similarly, the dq-axis inverter-voltage perturbations, $\Delta e_{d,n}, \Delta e_{q,n}$ and $\Delta e_{d,g}, \Delta e_{q,g}$ form the input vector, as defined in Eq. (2.18)

$$\mathbf{u}_{ur} = \left[\Delta e_{d,1}\ \Delta e_{q,1}\ \cdots\ \Delta e_{d,N}\ \Delta e_{q,N}\right]^\top \in \mathbb{R}^{2N}. \tag{2.18}$$

while the exogenous PCC input $\mathbf{w}_{ur}$ is defined in Eq. (2.16)

The resulting small-signal grid-interconnection model takes the compact form shown in Eq. (2.19):

$$\dot{\mathbf{x}}_{ur} \;=\; \mathbf{A}_{ur}\,\mathbf{x}_{ur} + \mathbf{B}_{Uur}\,\mathbf{u}_{ur} + \mathbf{B}_{Wur}\,\mathbf{w}_{ur}, \tag{2.19}$$

The matrices $\mathbf{A}_{ur}, \mathbf{B}_{Uur}, \mathbf{B}_{Wur}$ are assembled from the electrical line/cable and filter impedances expressed in the synchronous d–q frame and evaluated about the selected operating point. The corresponding interconnection structures is illustrated in 2

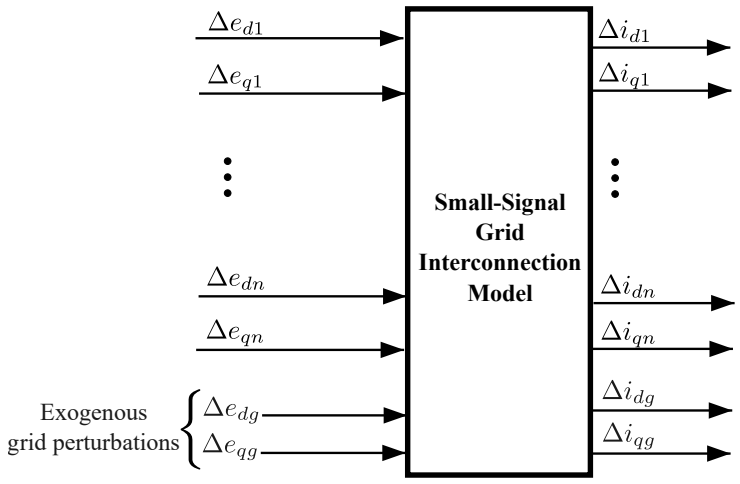

Figure 2: **Step D** — Grid interconnection model in the synchronous dq frame for grid-connected operation.

To maintain a common state space for the hybrid model, the ordering of $\mathbf{x}_{ur} \in \mathbb{R}^{2(N+1)}$ and inverter-voltage inputs $\mathbf{u}_{ur} \in \mathbb{R}^{2N}$ is retained in both operating modes, while the exogenous grid-voltage input is omitted. Therefore, the islanded MG model takes the form shown in Eq. (2.20):

$$\dot{\mathbf{x}}_{ur} \;=\; \mathbf{A}_{ur}^{\text{isl}}\,\mathbf{x}_{ur} + \mathbf{B}_{Uur}^{\text{isl}}\,\mathbf{u}_{ur}, \tag{2.20}$$

The matrix $\mathbf{A}_{ur}^{\text{isl}}$ is obtained from the same d–q impedance data but with the grid branch open (no coupling to $\mathbf{w}_{ur}$). This construction allows the integration of grid-connected and islanded cases to be represented within a single hybrid model that operates on the same state space.

E. Droop-controlled inverter small-signal model

A small-signal model is obtained for each droop-controlled inverter. The dynamics of the voltage and frequency of each inverter are considered, with the active and reactive power supplied by the inverter treated as inputs. A clear separation of time scales is assumed: the inner current and voltage loops are significantly faster than the droop loops and are Hurwitz, with bandwidth $\omega_{\text{inner}} \gg \omega_c$. Thus, the droop-loop states capture the slow dynamics. Under this assumption, the n-th inverter contributes three states: $\Delta\omega_n$, Δe_{dn} and Δe_{qn}; inputs are ΔP_n and ΔQ_n. Figure 3 shows the model for the n-th inverter with two inputs and three outputs.

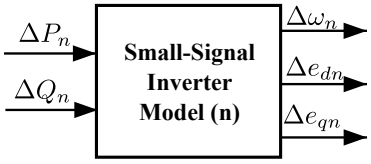

Figure 3: **Step E** — Small-signal droop model for the n-th inverter (two inputs, three outputs).

Using low-pass filtered power measurements with a cut-off of ω_c, the droop laws are

$$\omega = \omega_0 - k_p(P_{\text{flt}} - P_0), \quad E = E_0 - k_q(Q_{\text{flt}} - Q_0). \tag{2.21}$$

The linearized dynamics about the quiescent point can be expressed more succinctly as

$$\frac{d}{dt}\begin{bmatrix}\Delta x_d\\ \Delta x_q\\ \Delta x_\omega\end{bmatrix} = \mathbf{A}_{E\omega}\begin{bmatrix}\Delta x_d\\ \Delta x_q\\ \Delta x_\omega\end{bmatrix} + (\mathbf{A}_{E\omega}\mathbf{B}_{E\omega 0} + \omega_c\mathbf{B}_{E\omega 0})\begin{bmatrix}\Delta E_0\\ \Delta\omega_0\end{bmatrix} + \mathbf{B}_{PQ}\begin{bmatrix}\Delta P_{\text{inv}}\\ \Delta Q_{\text{inv}}\end{bmatrix}, \tag{2.22}$$

with outputs

$$\begin{bmatrix}\Delta E_d\\ \Delta E_q\\ \Delta\omega\end{bmatrix} = \begin{bmatrix}\mathbf{I}_3\end{bmatrix}\begin{bmatrix}\Delta x_d\\ \Delta x_q\\ \Delta x_\omega\end{bmatrix} + \mathbf{B}_{E\omega 0}\begin{bmatrix}\Delta E_0\\ \Delta\omega_0\end{bmatrix}. \tag{2.23}$$

Remark (GFM vs. GFL). The model above corresponds to grid-forming (GFM) operation, with no PLL inside the power plant; P–ω and Q–E droop control, consistent with recent usage [4, 12]. For grid-following (GFL) converters with PLL-based current control, the inverter-side outputs $(\Delta E_d, \Delta E_q, \Delta\omega)$ should be replaced by the corresponding current references $(\Delta i_d^\star, \Delta i_q^\star)$, and the grid interconnection should be updated in Step D accordingly, including the admittance map and input placement. The hybrid structure (C, f, D, g) and the PCC switching policy remain unchanged; only the local blocks that feed A_m, B_m are modified.

State accounting (consistency). In this work three droop states $(\Delta e_{dn}, \Delta e_{qn}, \Delta\omega_n)$ are associated with each inverter. Together with the *two* grid current states $(\Delta i_{dn}, \Delta i_{qn})$ already included in $\mathbf{x}_{ur}$ from Step D, this gives a total of **five** states per inverter within the common state space. Therefore, the overall continuous dimension is $n_x = 2 + 5N$.

E.1 Closed-loop output impedance of the droop-controlled inverter

Let $\Delta v_{\text{out}}(t)$ and $\Delta i_{\text{out}}(t)$ denote the small-signal perturbations of the inverter output voltage and current, respectively, at the PCC in the synchronous dq frame. Their Laplace transforms are denoted by $\Delta V_{\text{out}}(s)$ and $\Delta I_{\text{out}}(s)$. The closed-loop output impedance of the droop-controlled inverter is defined as

$$Z_{\text{out}}(s) := \frac{\Delta V_{\text{out}}(s)}{\Delta I_{\text{out}}(s)} \quad \text{with all other inputs held at their operating-point values.} \tag{2.24}$$

For the n-th inverter, the small-signal model in Section E can be expressed in compact state–space form as

$$\Delta\dot{x}_n(t) = A_n^{\mathrm{cl}}\,\Delta x_n(t) + B_n^{i}\,\Delta i_{\mathrm{out},n}(t) + B_n^{w}\,\Delta w_n(t), \tag{2.25a}$$

$$\Delta v_{\mathrm{out},n}(t) = C_n^{v}\,\Delta x_n(t) + D_n^{vi}\,\Delta i_{\mathrm{out},n}(t) + D_n^{vw}\,\Delta w_n(t), \tag{2.25b}$$

where Δx_n stacks the droop and grid states associated with inverter n, $\Delta i_{\mathrm{out},n}$ is the small-signal output current injection toward the PCC, and Δw_n collects exogenous perturbations, such as setpoint variations or upstream grid-voltage deviations. The matrix A_n^{cl} incorporates the effects of the droop controller and the power-measurement filter, making the dependence of $Z_{\mathrm{out}}(s)$ on the control design explicit.

By taking the Laplace transforms of Eqs. (2.25a)–(2.25b) and setting $\Delta w_n(s) \equiv 0$ for the impedance calculation, the resulting input–output map from $\Delta I_{\mathrm{out},n}(s)$ to $\Delta V_{\mathrm{out},n}(s)$ is given by

$$\Delta V_{\mathrm{out},n}(s) \;=\; \Big(C_n^{v}\,(sI - A_n^{\mathrm{cl}})^{-1}B_n^{i} + D_n^{vi}\Big)\,\Delta I_{\mathrm{out},n}(s). \tag{2.26}$$

Therefore, the closed-loop output impedance of the droop-controlled inverter, in small-signal form, is

$$Z_{\mathrm{out},n}(s) \;=\; C_n^{v}\,(sI - A_n^{\mathrm{cl}})^{-1}B_n^{i} + D_n^{vi}. \tag{2.27}$$

Expression (2.27) shows directly how the choice of droop gains, the power-measurement cutoff frequency, and any auxiliary control loops modify the apparent output impedance seen from the PCC. In particular, higher P–ω or Q–E droop gains tend to reduce the magnitude of $Z_{\mathrm{out},n}(s)$ at low frequencies, shifting the behavior from a more "voltage-source-like" (low damping) characteristic toward a more "impedance-shaped" and better damped response. This viewpoint is consistent with previous studies on closed-loop output impedance of droop-controlled inverters in islanded operation, such as the analysis in [16].

E.2 Equivalent PCC impedance in grid-connected and islanded modes

The unified small-signal model in Section H provides a common state vector x and mode-dependent matrices $A_{\mathrm{sis}}^{(m)}$, $m \in \{0,1\}$, for the grid-connected ($m = 0$) and islanded ($m = 1$) regimes. Let $\Delta v_{\mathrm{PCC}}(t)$ denote the small-signal voltage at the PCC and let $\Delta i_{\mathrm{PCC}}(t)$ denote the algebraic sum of the currents injected by the inverters and the grid branch (when present), with all currents oriented toward the PCC. Their Laplace transforms are denoted by $\Delta V_{\mathrm{PCC}}(s)$ and $\Delta I_{\mathrm{PCC}}(s)$, respectively.

The equivalent small-signal impedance observed at the PCC in mode m is defined as

$$Z_{\mathrm{eq}}^{(m)}(s) \;:=\; \frac{\Delta V_{\mathrm{PCC}}(s)}{\Delta I_{\mathrm{PCC}}(s)}, \qquad m \in \{0,1\}, \tag{2.28}$$

with all other independent perturbation inputs held at their operating-point values. Using the augmented state–space realization Eq. (2.43), the linearized dynamics around a given operating point can be written as

$$\Delta\dot{x}(t) = A_{\mathrm{sis}}^{(m)}\,\Delta x(t) + B_{\mathrm{sis}}\,\Delta u(t) + B_W^{(m)}\,\Delta w(t), \tag{2.29a}$$

$$\Delta v_{\mathrm{PCC}}(t) = C_{\mathrm{PCC}}^{v}\,\Delta x(t) + D_{\mathrm{PCC}}^{vu}\,\Delta u(t) + D_{\mathrm{PCC}}^{vw}\,\Delta w(t), \tag{2.29b}$$

$$\Delta i_{\mathrm{PCC}}(t) = C_{\mathrm{PCC}}^{i}\,\Delta x(t) + D_{\mathrm{PCC}}^{iu}\,\Delta u(t) + D_{\mathrm{PCC}}^{iw}\,\Delta w(t), \tag{2.29c}$$

where Δu collects control-related perturbations (e.g., setpoints), and Δw includes exogenous inputs, such as upstream grid-voltage deviations in grid-connected mode.

For the impedance computation, $\Delta u(s)$ and $\Delta w(s)$ are set to zero. Eqs. (2.29b)–(2.29c) can then be combined to obtain the following

$$Z_{\mathrm{eq}}^{(m)}(s) \;=\; \frac{C_{\mathrm{PCC}}^{v}\,(sI - A_{\mathrm{sis}}^{(m)})^{-1}B_{\mathrm{PCC}}^{i} + D_{\mathrm{PCC}}^{vi}}{C_{\mathrm{PCC}}^{i}\,(sI - A_{\mathrm{sis}}^{(m)})^{-1}B_{\mathrm{PCC}}^{i} + D_{\mathrm{PCC}}^{ii}}, \qquad m \in \{0,1\}, \tag{2.30}$$

where B_{PCC}^{i} and the direct-feedthrough terms $D_{\mathrm{PCC}}^{vi}, D_{\mathrm{PCC}}^{ii}$ are obtained from the assembled electrical-grid and inverter models (Steps D–F).

Equation (2.30) highlights how the equivalent PCC impedance changes between islanded and grid-connected operation through the mode-dependent matrices $A_{\mathrm{sis}}^{(m)}$ and $B_{W}^{(m)}$. In islanded mode ($m = 1$), the inverters and the local load dominate the impedance seen from the PCC, whereas in grid-connected mode ($m = 0$), the presence of the upstream grid branch tends to "stiffen" the PCC and reduce the magnitude of $Z_{\mathrm{eq}}^{(0)}(s)$ at low frequencies. This contrast is exploited in Section 5, where the Bode plots of $Z_{\mathrm{out},n}(s)$ and $Z_{\mathrm{eq}}^{(m)}(s)$ are presented and interpreted. In particular, the results show that the droop parameters and the power–measurement filters determine the apparent low–frequency stiffness of the converter and of the microgrid as a whole.

F. Small-signal relations for active and reactive power

Variations in the active and reactive power of each inverter are computed from small deviations in its voltage and current components around the quiescent operating point. Let the dq–components at the operating point be $\left(E_{d0,n}, E_{q0,n}, i_{d0,n}, i_{q0,n}\right)$ and the small deviations be $\left(\Delta E_{dn}, \Delta E_{qn}, \Delta i_{dn}, \Delta i_{qn}\right)$. Using the standard dq power definitions, the small-signal power relations are given by

$$\Delta P_n = \tfrac{3}{2}\left(i_{d0,n}\,\Delta E_{dn} + E_{d0,n}\,\Delta i_{dn} + i_{q0,n}\,\Delta E_{qn} + E_{q0,n}\,\Delta i_{qn}\right), \tag{2.31}$$

$$\Delta Q_n = \tfrac{3}{2}\left(i_{d0,n}\,\Delta E_{qn} + E_{d0,n}\,\Delta i_{dn} - i_{q0,n}\,\Delta E_{dn} - E_{d0,n}\,\Delta i_{qn}\right), \tag{2.32}$$

where the factor $\kappa = \frac{3}{2}$ is fixed for three-phase dq RMS magnitudes and is used consistently across all power computations in this paper. Equivalently, the model can be expressed in compact form as

$$\begin{bmatrix} \Delta P_n \\ \Delta Q_n \end{bmatrix} = \tfrac{3}{2}\begin{bmatrix} i_{d0,n} & i_{q0,n} & E_{d0,n} & E_{q0,n} \\ -\,i_{q0,n} & i_{d0,n} & -E_{q0,n} & -E_{d0,n} \end{bmatrix}\begin{bmatrix} \Delta E_{dn} \\ \Delta E_{qn} \\ \Delta i_{dn} \\ \Delta i_{qn} \end{bmatrix}. \tag{2.33}$$

Figure 4 shows how the small-signal voltage components from Step E, $\left(\Delta E_{dn}, \Delta E_{qn}\right)$, and the small-signal inverter current components from Step D, $\left(\Delta i_{dn}, \Delta i_{qn}\right)$, feed into a power-linearization block that yields $\left(\Delta P_n, \Delta Q_n\right)$. These quantities are then used as inputs to the n-th inverter droop model derived in Step E.

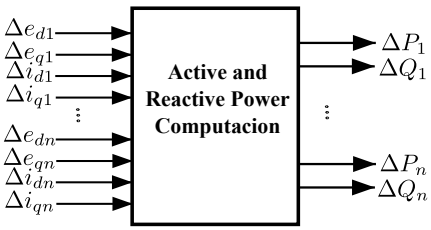

Figure 4: **Step F** — Linearization of active/reactive power around the operating point using dq small-signal variables.

In Fig. 5, the **E** blocks contain the small-signal droop models for each inverter, providing $(\Delta\omega_n, \Delta e_{dn}, \Delta e_{qn})$. The grid interconnection (**D** block) implements the linearized admittance map, translating nodal-voltage variations $(\Delta e_{dn}, \Delta e_{qn}, \Delta e_{dg}, \Delta e_{qg})$ into current variations $(\Delta i_{dn}, \Delta i_{qn}, \Delta i_{dg}, \Delta i_{qg})$. The **F** block computes the active/reactive perturbations $(\Delta P_n, \Delta Q_n)$ from $(\Delta \mathbf{e}_n, \Delta \mathbf{i}_n)$ about the quiescent point and feeds them back to the droop loops, thereby closing the modular feedback path. The vertical ellipsis denotes identical intermediate inverters $(2, \ldots, n-1)$ that are omitted for brevity, while grid-side perturbations $(\Delta e_{dg}, \Delta e_{qg})$ enter as exogenous inputs.

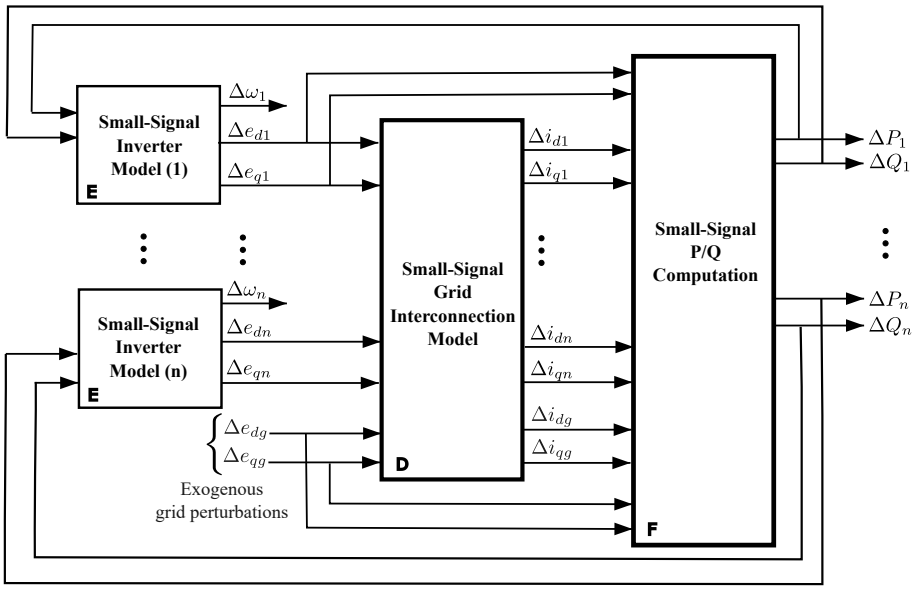

Figure 5: **Steps D–F** — Modeling framework: grid interconnection (D), inverter droop (E), and power linearization (F) assembled into a closed-loop small-signal representation.

G. Operating points (equilibria)

In grid-connected operation, the steady state of the grid interconnection is satisfied.

$$\mathbf{0} \;=\; \mathbf{A}_{ur}\,\mathbf{x}_{ur,0} \;+\; \mathbf{B}_{Uur}\,\mathbf{u}_{ur,0} \;+\; \mathbf{B}_{Wur}\,\mathbf{w}_{ur,0}, \tag{2.34}$$

where the steady-state vectors are collected as shown in Eq. (2.35):

$$\begin{aligned}\mathbf{x}_{ur,0} &= \left[i_{d0,1}\ i_{q0,1}\ \cdots\ i_{d0,N}\ i_{q0,N}\ i_{d0,g}\ i_{q0,g}\right]^\top,\\ \mathbf{u}_{ur,0} &= \left[E_{d0,1}\ E_{q0,1}\ \cdots\ E_{d0,N}\ E_{q0,N}\right]^\top,\\ \mathbf{w}_{ur,0} &= \left[E_{d0,g}\ E_{q0,g}\right]^\top.\end{aligned} \tag{2.35}$$

At the droop-control equilibria of the inverter,

$$\omega_{\text{grid}} = \omega_{0,n} - k_{p,n}(E_{d0,n}\, i_{d0,n} + E_{q0,n}\, i_{q0,n})\,, \tag{2.36}$$

$$\sqrt{E_{d0,n}^2 + E_{q0,n}^2} = E_{0,n} - k_{q,n}(E_{q0,n}\, i_{d0,n} - E_{d0,n}\, i_{q0,n})\,, \tag{2.37}$$

for $n = 1, \ldots, N$.

In islanded operation, the MG steady state reduces to

$$\mathbf{0} \;=\; \mathbf{A}_{ur}^{\text{isl}}\,\mathbf{x}_{ur,0} \;+\; \mathbf{B}_{Uur}^{\text{isl}}\,\mathbf{u}_{ur,0}, \tag{2.38}$$

with droop constraints

$$\omega = \omega_{0,n} - k_{p,n}(E_{d0,n}\, i_{d0,n} + E_{q0,n}\, i_{q0,n})\,, \tag{2.39}$$

$$\sqrt{E_{d0,n}^2 + E_{q0,n}^2} = E_{0,n} - k_{q,n}(E_{q0,n}\, i_{d0,n} - E_{d0,n}\, i_{q0,n})\,, \tag{2.40}$$

and the power balance

$$\sum_{n=1}^{N} P_{0,n} \;=\; \sum_{n=1}^{N} P_{\text{loss},n} \;+\; P_{\text{load}}, \qquad P_{0,n} = E_{d0,n}\, i_{d0,n} + E_{q0,n}\, i_{q0,n}. \tag{2.41}$$

H. Augmented small-signal model (both modes)

A single state vector with a fixed ordering is adopted, as shown in Eq. (2.42):

$$x \;:=\; \Big[\ \underbrace{\Delta i_{dg}\ \ \Delta i_{qg}}_{\text{grid currents}}\ \underbrace{(\Delta i_{d1}\ \Delta i_{q1}\ \ \Delta e_{d1}\ \Delta e_{q1}\ \Delta\omega_1)}_{\text{VSI1 (5)}}\ \cdots\ \underbrace{(\Delta i_{dN}\ \Delta i_{qN}\ \ \Delta e_{dN}\ \Delta e_{qN}\ \Delta\omega_N)}_{\text{VSIN (5)}}\ \Big]^\top \in \mathbb{R}^{2+5N}, \tag{2.42}$$

This ordering is used in both modes and in all hybrid maps. Let $\Delta\mathbf{u}_{\text{invs}}^{EW}$ collect exogenous E/ω setpoint perturbations, if any, and let $\Delta\mathbf{w}_{ur} = [\Delta e_{dg}\ \Delta e_{qg}]^\top$ denote PCC grid-voltage perturbations, which are present only in grid-connected operation. The closed-loop small-signal model is given in Eq. (2.43):

$$\dot{x} \;=\; A_{\text{sis}}^{(m)}\, x \;+\; B_{\text{sis}}\,\Delta\mathbf{u}_{\text{invs}}^{EW} \;+\; B_W^{(m)}\,\Delta\mathbf{w}_{ur}, \tag{2.43}$$

where $m \in \{0,1\}$ encodes the STS position (m=0 grid-connected, m=1 islanded), $A_{\text{sis}}^{(m)} \in \mathbb{R}^{(2+5N)\times(2+5N)}$, and $B_{\text{sis}} \in \mathbb{R}^{(2+5N)\times n_u}$. By construction, the mode-dependent matrices in Eq. (2.44) satisfy

$$B_W^{(m)} \;=\; (1-m)\,B_W, \qquad A_{\text{sis}}^{(m)} \;=\; A_{\text{sis}}^{\text{grid}} \;+\; m\Big(A_{\text{sis}}^{\text{isl}} - A_{\text{sis}}^{\text{grid}}\Big)\,, \tag{2.44}$$

where $A_{\text{sis}}^{\text{grid}}$ and $A_{\text{sis}}^{\text{isl}}$ arise from Steps D–F after linearizing at the mode-wise operating points (Sec. G) and assembling: (i) the grid admittance map (current rows/columns), (ii) the droop dynamics (voltage/frequency rows/columns), and (iii) the power-linearization feedback (gain blocks from $(\Delta\mathbf{e}_n, \Delta\mathbf{i}_n)$ to $(\Delta P_n, \Delta Q_n)$).

I. Unified hybrid realization on a common state

By combining the hybrid structure introduced in Eq. (2.1) with the augmented small-signal model of Step H, the inverter-based microgrid is described as a hybrid system, with its state defined in Eq. (2.45):

$$z := (x, m, \tau) \in \mathbb{R}^{n_x} \times \{0, 1\} \times \mathbb{R}_{\geq 0}, \tag{2.45}$$

where $x \in \mathbb{R}^{n_x}$ stacks the continuous variables of the grid and the droop-controlled inverters, m encodes the STS position (m=0 grid-connected, m=1 islanded), and τ denotes the dwell-time accumulator.

The mode-dependent closed-loop matrices can be succinctly expressed as

$$A_{\text{sis}}^{(0)} := A_{\text{sis}}^{\text{grid}}, \qquad A_{\text{sis}}^{(1)} := A_{\text{sis}}^{\text{isl}}, \tag{2.46}$$

so that

$$A_{\text{sis}}^{(m)} = A_{\text{sis}}^{\text{grid}} + m\big(A_{\text{sis}}^{\text{isl}} - A_{\text{sis}}^{\text{grid}}\big), \qquad m \in \{0, 1\}, \tag{2.47}$$

with $A_{\text{sis}}^{\text{grid}}, A_{\text{sis}}^{\text{isl}} \in \mathbb{R}^{n_x \times n_x}$ obtained from the procedure in Steps D–H for the operating points considered in Sec. 4. The input matrix B_{sis} does not depend on the mode, whereas the grid-voltage coupling is present only in grid-connected operation, thus $B_W^{(m)} = (1 - m)\, B_W$.

Flow map. Using the notation of Eq. (2.43), the flow dynamics of the hybrid model can be expressed as

$$\dot{x} = A_{\text{sis}}^{(m)}\, x + B_{\text{sis}}\, \Delta \mathbf{u}_{\text{invs}}^{EW} + (1 - m)\, B_W\, \Delta \mathbf{w}_{ur}, \quad \dot{m} = 0, \quad \dot{\tau} = 1, \qquad z \in C, \tag{2.48}$$

where the flow and jump sets C and D are given in Eqs. (2.13a)–(2.13b) in terms of the hysteretic functions ϕ_{open} and ϕ_{close}.

Jump map (STS toggling with affine realignment). Let $x_m^\star$ be the operating point of mode m computed in Subsection G. To preserve the continuity of the incremental coordinates $\tilde{x} := x - x_m^\star$ at STS commutations, an affine reset is adopted.

$$x^+ = x + \big(x_{1-m}^\star - x_m^\star\big), \qquad m^+ = 1 - m, \qquad \tau^+ = 0, \qquad z \in D, \tag{2.49}$$

so that $\tilde{x}^+ = \tilde{x}$ is continuous across the jump. The jump set D is also defined in Eq. (2.13) and enforces both the hysteretic conditions at the PCC and the minimum dwell time $\tau_{\min}$.

Summary. Equations Eq. (2.48), Eq. (2.49) together with the sets Eq. (2.13) and the mode-dependent matrices Eq. (2.46) provide a unified hybrid description of the MG in a single state space. This realization is independent of the particular choice of continuous coordinates and, under the time-scale separation assumptions stated in Sec. 3, is amenable to switched-system stability tools (e.g., Lie-algebraic and CQLF tests) applied to the pair $\{A_{\text{sis}}^{\text{grid}}, A_{\text{sis}}^{\text{isl}}\}$.

3. Stability analysis of the unified hybrid model

Proposición 3.1 (GUAS with CQLF for the switched pair)**.** *If a symmetric matrix $P = P^\top > 0$ and a scalar $\varepsilon > 0$ can be found such that the matrix inequalities in Eq. (3.1) are satisfied, namely*

$$A_0^\top P + P A_0 \leq -\varepsilon I, \qquad A_1^\top P + P A_1 \leq -\varepsilon I, \tag{3.1}$$

then the switched system $\dot{x} = A^{(m)}x$ is globally uniformly asymptotically stable (GUAS) under any switching signal $m(t) \in \{0, 1\}$.

Idea (sketch of proof). The quadratic candidate $V(x) = x^\top Px$ is considered, and it is verified that $\dot{V} \leq -\varepsilon\|x\|^2$ in each mode; continuity of the incremental state at jumps is then used to conclude GUAS.

From a practical perspective, these conditions complement the modal metrics reported in Table 2. While the eigenvalues of $A_{\text{sis}}^{(0)}$ and $A_{\text{sis}}^{(1)}$ quantify local damping in each mode, the CQLF-based test provides a sufficient certificate for arbitrary switching between the two modes, that is under the actual STS switching logic. Thus, planned islanding and reconnection can be interpreted as *seamless* transitions of a GUAS switched system rather than as independent operating cases.

4. Case study and results

A laboratory–scale microgrid with two three-phase VSIs supplying an RL load through a PCC equipped with an STS is considered (cf. Fig. 1). Representative electrical and control parameters are given in Table 1. The synchronous frame rotates at $\omega_0 = 2\pi \cdot 60\,\text{Hz}$ and RMS conventions are used consistently. When required, the $3/2$ scaling for three-phase dq transformations is consistently applied across power computations.

Operating points and linearization

Steady-state operating points are obtained by solving the algebraic grid-interconnection equations along with the droop constraints (see Subsection G). Linearizing around these operating points, the closed-loop small-signal model is derived as presented in Eq. (2.43). For $N = 2$, voltage source inverters (VSIs) are utilized, the common state dimension amounts to $2 + 5N = 12$. This includes two grid-current states along with five states for each inverter.

PCC thresholds and dwell time

The switching logic uses the hysteretic functions defined in Eqs. (2.12a)–(2.12b). The thresholds are selected such that $\omega_{\text{open}} > \omega_{\text{close}} > 0$, $E_{\text{open}} > E_{\text{close}} > 0$, $\theta_{\text{close}} > 0$, and $\tau_{\min} > 0$, with representative values selected according to interconnection standards and the characteristics of the laboratory hardware.

5. Results

Simulation scenarios and setup

The laboratory–scale microgrid described in Section 4, consisting of $N = 2$ three-phase VSIs feeding an RL load through a PCC equipped with an STS, is considered. The continuous dynamics are governed by the unified hybrid realization in Eq. (2.48)–Eq. (2.49), with the mode matrices $A_{\text{sis}}^{(0)}$ (grid-connected) and $A_{\text{sis}}^{(1)}$ (islanded) obtained as in Steps D–H. Representative electrical and control parameters are summarized in Table 1.

Three simulation scenarios are evaluated:

1. **S1 (Grid-connected, small perturbation):** the MG operates in grid-connected mode ($m = 0$) while a small step is applied to $(\Delta e_{dg}, \Delta e_{qg})$, emulating a perturbation in the upstream grid.
2. **S2 (Islanding):** starting from the steady state of S1, the STS opens when the mismatch function $\phi_{\text{open}}(x)$ in Eq. (2.12a) becomes nonnegative and the dwell-time condition $\tau \geq \tau_{\min}$ is satisfied. The system then evolves with $m = 1$.
3. **S3 (Reconnection):** from the islanded steady state, the MG is resynchronized with the grid. Closing is enabled when $\phi_{\text{close}}(x) \geq 0$ in Eq. (2.12b) and $\tau \geq \tau_{\min}$; at that instant, the STS closes ($m \leftarrow 0$), and the hybrid jump map realigns the operating point as in Eq. (2.49).

Unless otherwise stated, the typical synchronization thresholds $(\omega_{\text{open}}, E_{\text{open}}) = (2\,\omega_{\text{close}}, 2\,E_{\text{close}})$ and $\theta_{\text{close}} = 5^\circ$ are adopted, along with $\tau_{\min} = 120\,\text{ms}$, consistent with the laboratory hardware and interconnection practices.

Table 1: Power system characteristics (representative).

Grid voltage	120 V_{RMS}, 60 Hz
Line (Inv1) (R, L)	12.0 mΩ, 120 µH
Line (Inv2) (R, L)	12.0 mΩ, 120 µH
Line (Grid) (R, L)	30.0 mΩ, 304 µH
Load (R, L)	7.4483 Ω, 7.903 mH
Droop k_p (both)	0.0286 Hz/kW
Droop k_q (both)	0.300 V_{RMS}/kVAr
Setpoints (E_0, ω_0)	see text
Filter cut-off f_c	5.0 Hz ($\omega_c = 2\pi f_c$)

Active/reactive power and STS status

Figure 6 shows the active and reactive powers of the load, the two inverters, and the grid over the entire simulation horizon, along with the STS status. The upper and middle panels correspond to active and reactive powers, respectively, while the bottom panel reports the STS position, highlighting the islanded interval between the opening at $t \approx 4$ s (transition S1→S2) and the closing at $t \approx 9$ s (transition S2→S3).

Before islanding, the load active and reactive powers (P_L, Q_L) are jointly supplied by the inverters, while the grid contribution remains negligible. At $t \approx 4$ s the STS opens, forcing a sudden change in the boundary conditions. As shown in the upper and middle panels of Fig. 6, this produces short, well-damped oscillations in the individual inverter powers, consistent with the instantaneous mismatch between the pre-fault grid phasor and the islanded droop references. After a brief transient, the system settles to a new sharing point determined by the droop coefficients, with no sustained oscillations or secondary peaks. These results indicate that the proposed hybrid realization provides an orderly transition to islanded operation while maintaining power balance and avoiding large excursions in P or Q.

When the synchronization window is satisfied and the dwell-time requirement is met, the STS closes at $t \approx 9$ s, reconnecting the MG to the grid. As shown in Fig. 6, he active and reactive powers

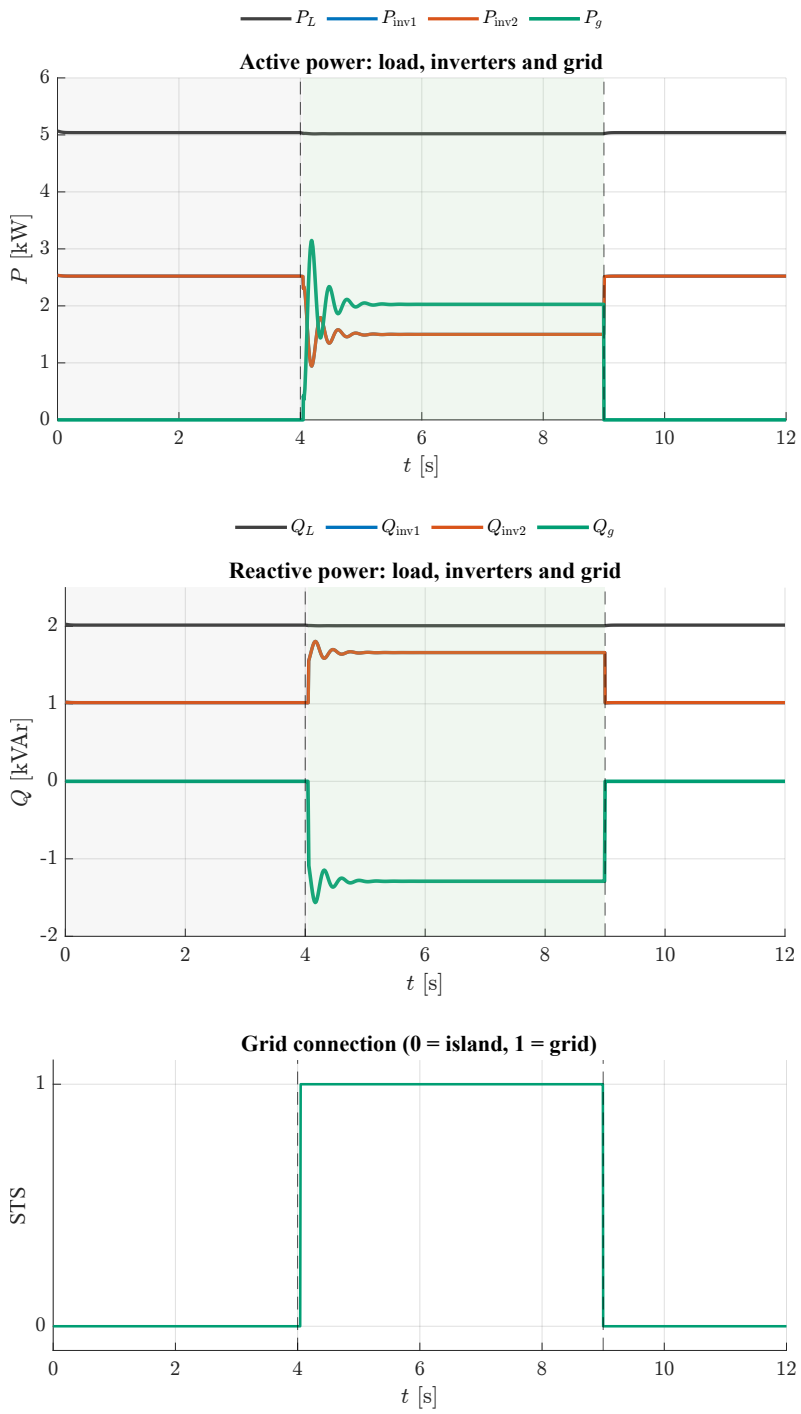

Figure **6**: Active and reactive power of the load, inverters and grid, and STS status over the full simulation horizon.

adjust smoothly to the new operating point: the grid resumes supplying part of the load while the inverter injections shift toward their grid-connected values without overshoot or oscillatory behavior. The absence of abrupt power reversals or high-frequency components confirms the effectiveness of the

synchronization and dwell-time logic, ensuring that the mismatches in voltage, phase, and frequency are negligible at the moment of closing. Consequently, the reconnection is executed as a controlled, low-stress event for both the inverters and the grid interface.

Voltage magnitude, phase, and frequency at the PCC

Figures 8 and 7 summarize the behavior of voltage magnitude, phase, and frequency at the PCC during the planned islanding and reconnection sequences. In both figures, the top panels display the RMS voltages at the inverters and the PCC, the middle panels report the phase-error signals $(\Delta\phi_1, \Delta\phi_2)$ relative to the grid, and the bottom panels show the inverter frequencies (ω_1, ω_2).

Before the STS opens, the PCC voltage closely tracks the grid reference, and both inverters operate with almost identical RMS magnitudes. In the phase plots of Figs. 8 and 7, the middle panels present the phase-error signals $(\Delta\phi_1, \Delta\phi_2)$ that remain tightly clustered around zero, indicating that the droop loops and the virtual grid phasor used for synchronization are well aligned. Consistently, the frequency trajectories in both figures stay close to ω_0, with only minor deviations caused by the active-power droop action and the grid perturbation in S1.

Figure 8 focuses on the islanding event S1–S2. Once the STS opens at $t \approx 4$ s, the PCC is solely driven by the droop-controlled inverters, and its RMS voltage converges to the islanded operating point without any overshoot. The phase errors are measured relative to the same "virtual" grid phasor and drift smoothly as the island evolves in free-running mode, while the inverter frequencies settle to a common value slightly offset from ω_0 according to the active-power droop law.

Figure 7 complements this view by zooming on the reconnection phase S2–S3. During this interval, the synchronization logic steers both the voltage magnitude and the inverter frequencies back towards the grid values: the trajectories of ω_1, ω_2 are brought close to ω_0, and the phase errors $(\Delta\phi_1, \Delta\phi_2)$ are driven back to a small neighborhood of zero. At the closing instant (around $t \approx 9$ s), the mismatch in phase and frequency is therefore small, which explains the absence of noticeable voltage or frequency transients in the subsequent grid-connected regime.

Synchronization window and dwell-time enforcement

Figure 9 details the behavior of the synchronization variables and the associated dwell-time logic during reconnection. The first three panels display the absolute mismatches $|\Delta\phi|$, $|\Delta\omega|$ and $|\Delta E|$ accompanied by their prescribed bounds. After islanding, these errors evolve freely as the microgrid operates in islanded mode; when the reconnection phase starts, the hybrid controller gradually drives them inside the "close window" $\mathcal{W}_{\text{on}}$, ensuring that phase, frequency, and voltage are simultaneously within acceptable tolerance limits before any closing actions are permitted.

The fourth panel displays the accumulated time in band $s(t)$, which grows only while all three mismatches remain inside $\mathcal{W}_{\text{on}}$. The bottom panel shows the dwell timer τ together with the STS state. A closing jump is triggered only when both conditions are met: (i) the logical function $\phi_{\text{close}}(x) \geq 0$ (all mismatches in band), and (ii) $s(t)$ has exceeded the required dwell time while $\tau \geq \tau_{\min}$. This dual timing mechanism effectively mitigates spurious or rapid switching, minimizes sensitivity to measurement noise, and ensures that reconnection occurs as a well-separated, low-stress event for both the inverters and the upstream grid.

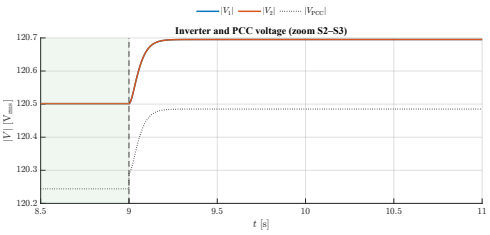

(a) Inverter and PCC voltage around reconnection (S2–S3).

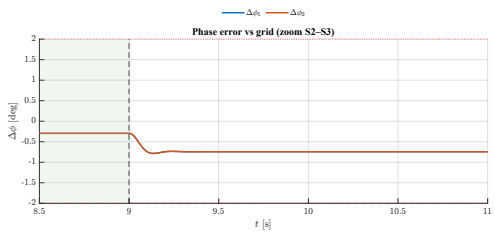

(b) Phase error with respect to the grid around reconnection (S2–S3).

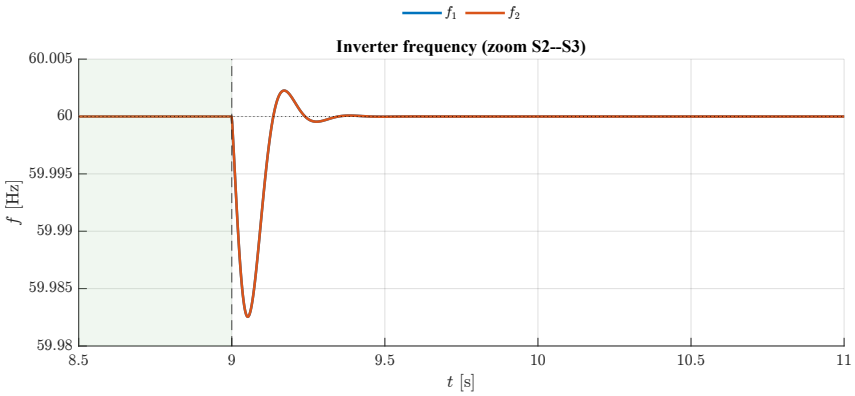

(c) Inverter frequency around reconnection (S2–S3).

Figure 7: RMS voltages, phase error, and inverter frequency during the planned reconnection (S2–S3). The change of mode occurs at $t \approx 9$ s, as indicated by the vertical event markers in each panel.

Stability assessment

To complement the time-domain experiments, the local linearizations of the hybrid model around the operating points of the islanded and grid-connected modes were examined. For each mode $m \in \{0, 1\}$, the Jacobian $A_{\text{sis}}^{(m)}$ was computed at the corresponding steady state, and its spectrum was summarized in Table 2 in terms of the largest real part and the smallest damping ratio. In both cases, all eigenvalues lie in the open left half-plane, with dominant real parts on the order of $\mathcal{O}(10)\,\text{s}^{-1}$ and damping ratios well above typical minimum design thresholds. This is consistent with the smooth active/reactive power trajectories in Fig. 6 and the well-behaved voltage, phase, and frequency responses in Figs. 8 and 7.

The additional linearization associated with the synchronization dynamics (the "synchronization" row in Table 2) also exhibits comfortable margins, ensuring that the virtual grid phasor used for phase and frequency alignment does not introduce lightly damped modes. Altogether, the modal analysis supports the qualitative picture given by the simulations: the closed-loop system has sufficient damping in each mode, and the switching logic with thresholds and minimum dwell time prevents excessively fast commutations, leading to the well-separated, low-stress islanding and reconnection events observed in Figs. 6 and 9.

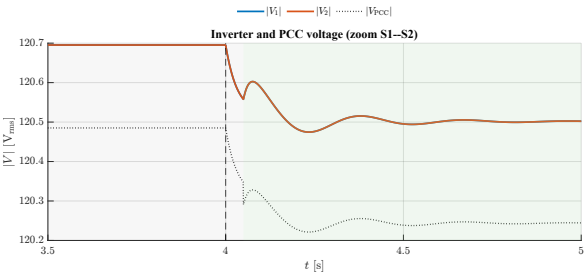

(a) Inverter and PCC voltage around islanding (S1–S2).

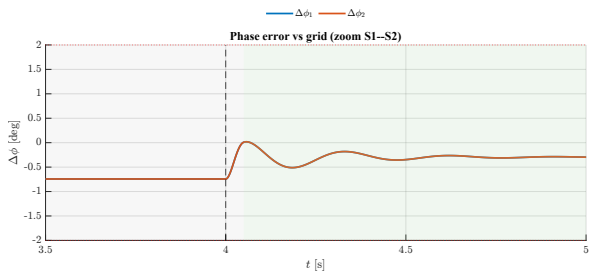

(b) Phase error with respect to the grid (S1–S2).

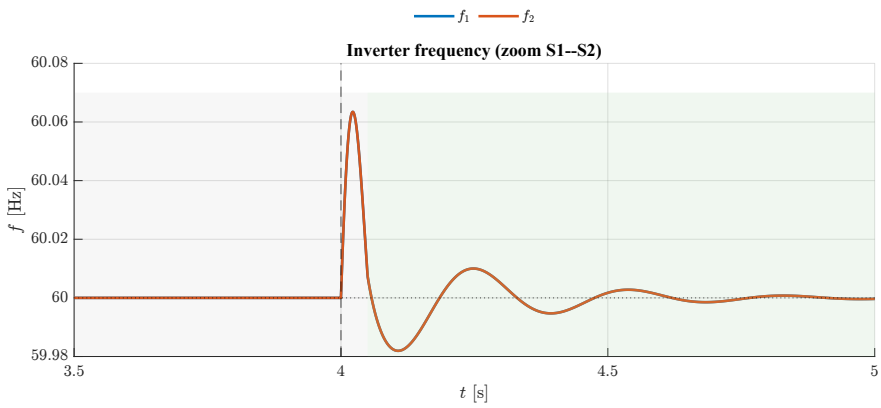

(c) Inverter frequency around islanding (S1–S2).

Figure 8: RMS voltages, phase error and inverter frequency during the planned islanding event (S1–S2). The dashed vertical line marks the STS opening at $t \approx 4$ s, and the window $[3{,}5,\ 5{,}0]$ s highlights the transient until the system settles to the islanded operating point.

Table 2: Representative eigenvalue metrics for each operating mode.

Mode	$\max \Re\{\lambda\}$ [s^{-1}]	$\min \zeta$
Islanded ($m = 1$)	$-31{,}42$	$0{,}60$
Grid-connected ($m = 0$)	$-5{,}69$	$0{,}28$

Closed-loop PCC impedance: Bode plot

To complement the time-domain and modal results, the closed-loop equivalent PCC impedance $Z_{\text{eq}}^{(m)}(s)$ was computed from the state-space realization of the droop-controlled inverters and the grid-side network model detailed in Sections E.1–E.2. Figure 10 presents the corresponding magnitude and phase Bode plots for islanded ($m = 1$) and grid-connected ($m = 0$) operation.

At low frequencies, the behavior of $Z_{\text{eq}}^{(m)}(s)$ reflects the combined effect of the P–ω and Q–E droop gains and the power-measurement low-pass filter. For the parameters of Table 1, the magnitude of $Z_{\text{eq}}^{(m)}(s)$ remains essentially flat around $1\,\Omega$, while the phase stays within a few tenths of a degree. At the fundamental frequency (60 Hz), the impedance is approximately $Z_{\text{eq}}^{(m)} \approx 1{,}0\,\Omega\angle{-0{,}1}^\circ$ in both operating modes. Thus, the converters behave as an almost purely resistive source when viewed from the PCC.

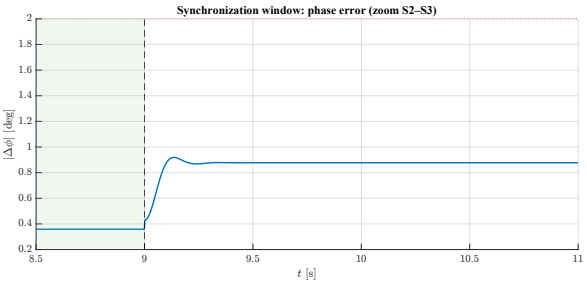

(a) Phase mismatch $|\Delta\phi|$ (zoom S2–S3).

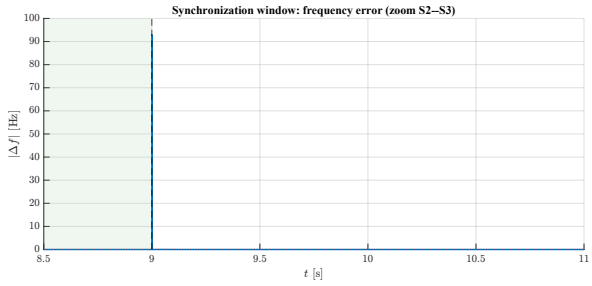

(b) Frequency mismatch $|\Delta f|$ (zoom S2–S3).

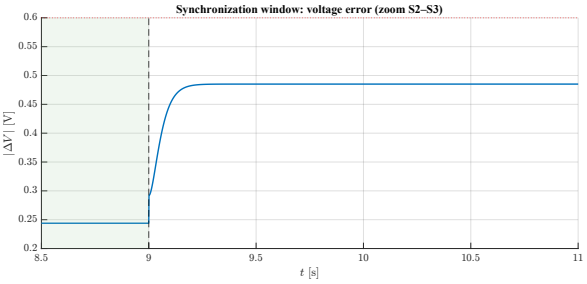

(c) Voltage mismatch $|\Delta V|$ (zoom S2–S3).

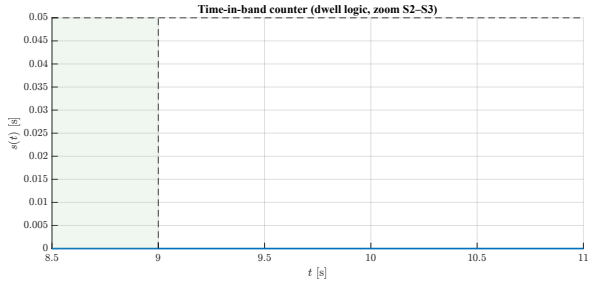

(d) Time-in-band $s(t)$ (dwell logic, zoom S2–S3).

Figure **9**: Synchronization window and dwell-time enforcement around the planned reconnection (S2–S3): (a) phase mismatch $|\Delta\phi|$, (b) frequency mismatch $|\Delta\omega|$, (c) voltage mismatch $|\Delta V|$, and (d) time-in-band counter $s(t)$.

The grid-connected case exhibits a slightly smaller magnitude and a marginally more lagging phase, reflecting the increased stiffness introduced by the upstream grid branch. These trends are consistent with the smooth islanding and reconnection trajectories reported in Figs. 6, 8 , and 7, and confirm that the selected droop parameters shape the low-frequency closed-loop impedance to be predominantly resistive.

6. Discussion

The numerical simulations confirm that the unified hybrid model produces consistent and well-behaved trajectories across both grid-connected and islanded operating modes, including the transitions managed by the static transfer switch (STS). Quantitative performance indicators extracted from the simulated responses directly support these observations.

During islanded operation (3.5–4.5 s), the load demand of approximately 5.0 kW is supplied entirely by the two inverters, which settle at steady-state powers of 1.57 kW each, as reported in Table 2. The frequency deviation remains small, with a maximum of $0{,}064$ Hz, while the maximum deviation in PCC voltage magnitude is limited to $0{,}49\ \mathrm{V_{rms}}$. The phase displacement between the inverter voltage and the notional grid reference remains below $0{,}74°$ throughout the window. These bounded deviations indicate stable operation and validate the droop-based power sharing mechanism under islanded conditions, consistent with the small-signal structure in Eq. (2.43).

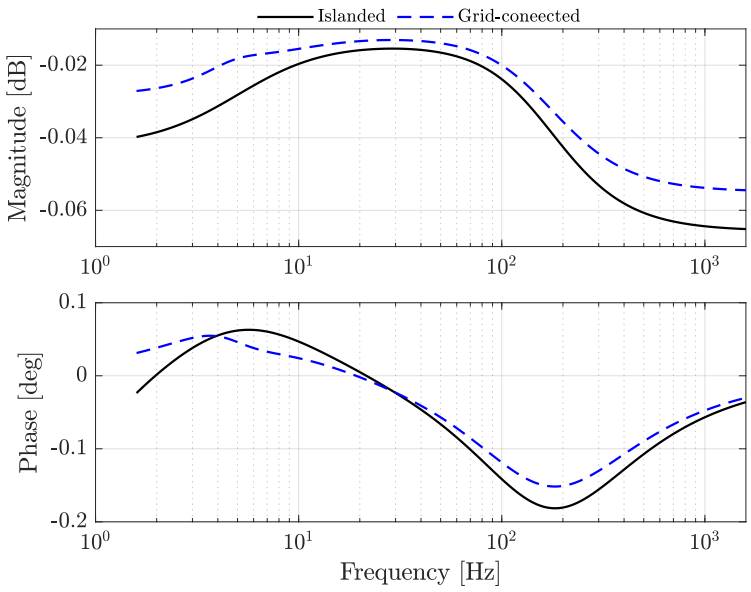

Figure **10**: Closed-loop equivalent PCC impedance $Z_{\mathrm{eq}}^{(m)}(j\omega)$ in islanded ($m = 1$) and grid-connected ($m = 0$) operation.

During the reconnection interval (8.5–9.5 s), the same load demand is shared between the grid and the inverters. After synchronization, both inverters converge to $2{,}52$ kW with zero overshoot, and the simulated grid contribution remains at 0 kW, reflecting the assumed power-flow direction. Again, the deviations remain small: the maximum frequency excursion is $0{,}018$ Hz, and the maximum voltage deviation at the PCC remains at $0{,}49$ $\mathrm{V_{rms}}$. The phase error at the PCC stays below $0{,}79°$, consistent with the prescribed synchronization bounds.

The synchronization metrics further confirm the effectiveness of the supervisory logic. The STS closing delay is only 50 ms, and the maximum phase mismatch at the closing event is approximately $0{,}92°$, with the voltage mismatch limited to $0{,}49$ $\mathrm{V_{rms}}$. These quantitative values demonstrate that the system adheres to the imposed guard and dwell-time conditions, achieving a smooth reconnection without transient power peaks in P_g or Q_g.

From a stability perspective, the modal analysis in Table 2 shows that both grid-connected and islanded linearizations have negative real eigenvalues and moderate damping, which supports the local asymptotic stability of each mode. This, together with the CQLF-based argument in Section 3, provides a sufficient certificate for GUAS of the switched system under the given logic.

Overall, the combination of small frequency and voltage deviations, bounded phase errors, and the absence of power overshoots during reconnection provides strong quantitative evidence that the unified hybrid model serves as an effective foundation for controller validation and microgrid supervisory studies.

These observations are fully consistent with the time-domain trajectories presented in Figures 6–9, where the islanding and reconnection events appear as well-separated, low-stress transitions with bounded deviations in all monitored variables.

7. Conclusions

A unified hybrid modeling methodology is introduced that captures both islanded and grid-connected operation of inverter-based microgrids within a single state-space representation with explicit switching logic. The approach supports stability certification through common quadratic Lyapunov arguments and allows the supervisory logic to be embedded directly within the dynamical model.

Quantitative results from the case study confirm the effectiveness of the proposed methodology. During islanded operation, the inverters restored a new equilibrium at approximately $1{,}57$ kW each, supplying a $5{,}02$ kW load, with frequency and voltage deviations limited to $0{,}064$ Hz and $0{,}49$ V_{rms}, respectively. During reconnection, the STS closed after 50 ms with the maximum phase mismatch below $1°$, yielding a smooth transition without power overshoot. Post-transition steady-state powers of $2{,}52$ kW per inverter were reached with zero overshoot, while frequency and voltage deviations remained below $0{,}018$ Hz and $0{,}49$ V_{rms}. These small deviations validate the synchronization logic and the robustness of the droop-based controller tuning.

The eigenvalue analysis further complements these findings, showing negative real parts and acceptable damping ratios for both operating modes, thus supporting the underlying stability claims. The hybrid model therefore provides a coherent platform for systematic controller design, tuning, and validation, and its modular structure enables straightforward extension to multiple inverters, different droop laws, or alternative supervisory strategies.

Future work will be devoted to studying operation under weaker grid conditions, unbalanced or nonlinear loads, and to performing experimental validation using hardware-in-the-loop platforms. These extensions will be built on the same hybrid structure, reinforcing the proposed model as a practical and scalable tool for design, analysis, and real-time supervisory control in inverter-dominated microgrids.

8. Contribution of authors

All authors contributed equally to the work, including writing, review, and editing.

9. Statement on Artificial Intelligence

AI was not used during the preparation of this work.

References

[1] I. Ahmed, M. Rehan, A. Basit, H. Ahmad, W. Ahmed, N. Ullah, M. Piecha, V. Blazek, and L. Prokop, "Review on microgrids design and monitoring approaches for sustainable green energy networks," *Scientific Reports*, vol. 13, 2023, https://doi.org/10.1038/s41598-023-48985-7.

[2] M. Uddin, H. Mo, D. Dong, S. Elsawah, J. Zhu, and J. M. Guerrero, "Microgrids: A review, outstanding issues and future trends," *Energy Strategy Reviews*, vol. 49, p. 101127, 2023, https://doi.org/10.1016/j.esr.2023.101127.

[3] M. Almihat, M. Abuzneid, M. Aljarrah, R. Telfah, and M. Hamarsheh, "An overview of ac–dc microgrid energy management systems," *AIMS Energy*, vol. 11, no. 6, pp. 1031–1069, 2023, https://doi.org/110.3934/energy.2023049.

[4] V. V. Babu, J. P. Roselyn, C. Nithya, and P. Sundaravadivel, "Development of grid-forming and grid-following inverter control in microgrid network ensuring grid stability and frequency response," *Electronics*, vol. 13, no. 10, 2024, https://doi.org/10.3390/electronics13101958.

[5] S. Peiris, S. Filizadeh, and D. Muthumuni, "Modular dynamic phasor modeling and simulation of renewable integrated power systems," *Energies*, vol. 17, no. 11, 2024, https://doi.org/10.3390/en17112480.

[6] N. Guruwacharya, S. Chakraborty, G. Saraswat, R. Bryce, T. M. Hansen, and R. Tonkoski, "Data-driven modeling of grid-forming inverter dynamics using power hardware-in-the-loop experimentation," *IEEE Access*, vol. 12, pp. 52 267–52 282, 2024, https://doi.org/10.1109/ACCESS.2024.3383323.

[7] A. Hmad, M. Barara, S. E. Hani, and M. Fraihi, "Review of mode transition process from grid-connected to standalone operation in microgrids based on voltage source inverters," *Energies*, vol. 16, no. 13, 2023, https://doi.org/10.3390/en16135062.

[8] J. Wang, S. Ganguly, and B. Kroposki, "Study of seamless microgrid transition operation using grid-forming inverters," in *Proc. 49th Annual Conference of the IEEE Industrial Electronics Society (IECON)*, Singapore, Oct. 2023, nREL preprint NREL/CP-5D00-86102. https://doi.org/10.1109/IECON51785.2023.10312287.

[9] I. Rai and S. C., "Microgrid and grid synchronization: A critical analysis of challenges and opportunities," *Electric Power Systems Research*, vol. 242, p. 111434, 2025, https://doi.org/10.1016/j.epsr.2025.111434.

[10] M. C. Merchan-Riveros and C. Albea, "Three time-scale singular perturbation hybrid control and large-signal analysis stability in ac-microgrids," *IEEE Transactions on Circuits and Systems I: Regular Papers*, vol. 70, no. 8, pp. 3373–3386, 2023, https://doi.org/10.1109/TCSI.2023.3273814.

[11] E. A. Pineda Muñoz and A. Gauthier Sellier, "Comparative study of three control strategies for the frequency regulation of an islanded microgrid," *Ingeniería*, vol. 25, no. 2, pp. 179–193, Jul. 2020, https://doi.org/10.14483/23448393.16144.

[12] B. Bahrani, M. H. Ravanji, B. Kroposki, D. Ramasubramanian, X. Guillaud, T. Prévost, and N.-A. Cutululis, "Grid-forming inverter-based resource research landscape: Understanding the key assets for renewable-rich power systems," *IEEE Power & Energy Magazine*, vol. 22, no. 2, pp. 18–31, 2024, https://doi.org/10.1109/MPE.2023.3343338.

[13] A. Mahdavian, A. A. Ghadimi, and M. Bayat, "Microgrid small-signal stability analysis considering dynamic load model," *IET Renewable Power Generation*, vol. 15, pp. 2799–2813, 2021,

https://doi.org/10.1049/rpg2.12203. [Online]. Available: https://digital-library.theiet.org/doi/abs/10.1049/rpg2.12203

[14] R. Goebel, R. G. Sanfelice, and A. R. Teel, *Hybrid Dynamical Systems: Modeling, Stability, and Robustness*. Princeton, NJ: Princeton University Press, 2012, https://doi.org/10.23943/princeton/9780691153896.001.0001.

[15] E. P. Correa, M. Mezaroba, and G. M. S. Azevedo, "Reduced-order small-signal model of ac microgrid for stability analysis and adjustment of droop control," in *Proceedings of an IEEE Conference*. IEEE, 2017, https://doi.org/10.1109/COBEP.2017.8257293.

[16] C. L. T. Rodríguez, D. V. de la Fuente, E. F. Amorós, G. G. Sanfeliú, and R. O. González, "Análisis de la impedancia de salida en lazo cerrado de inversores funcionando en modo isla, utilizando esquemas droop," *Ingeniería*, vol. 14, no. 2, pp. 4–12, 2009, output impedance analysis in a closed loop of inverters connected in parallel operating in island mode (in Spanish). https://doi.org/10.14483/23448393.2374.

Author biographies

A. D. J. Chica Leal received the B.S. degree in Electronic Engineering from the Universidad Autónoma de Colombia, Bogotá, Colombia, in 2002, and the M.Sc. degree from the Universidad de los Andes, Bogotá, Colombia, in 2008. He is currently pursuing the Ph.D. degree at the Universidad Distrital Francisco José de Caldas, Bogotá, Colombia. His research interests include power electronics and the modeling and control of microgrids.

C. L. Trujillo Rodríguez received the B.S. degree in Electronics Engineering (2003), M.Sc. in Electrical Engineering (2006), and Ph.D. in Electronics Engineering (2012). He is a Full Professor at Universidad Distrital Francisco José de Caldas. His interests include modeling and control of power converters for distributed generation and microgrids.

F. Santamaría received the B.S. (2003), M.S. (2007), and Ph.D. (2013) degrees in Electrical Engineering from Universidad Nacional de Colombia. He is a Full Professor at Universidad Distrital Francisco José de Caldas. His interests include electromagnetic compatibility, energy management, and electric vehicles.